High-resolution self-powered photodetector arrays based on vertical Au/PbI_2/ITO structures for advanced optoelectronic imaging

Lulu Huang(黄璐璐)[1], Wenjiao Yuan(苑文娇)[1], Huawei Liu(刘华伟)[1], Tanghao Xie(谢瑭皓)[1], Xiaoli Zhu(朱小莉)[1,†], Dong Li(李东)[1], and Anlian Pan(潘安练)[1,2,‡]

[1] *College of Materials Science and Engineering, Hunan University, Changsha* 410082, *China*
[2] *School of Physics and Electronics, Hunan Normal University, Changsha* 410081, *China*

(Received 20 September 2025; revised manuscript received 3 December 2025; accepted manuscript online 9 December 2025)

With the growing demand for photodetector (PD) arrays with high pixel counts, enhanced sensitivity, faster response, and simplified fabrication processes, traditional PD designs based on planar interdigital electrodes or two-device integration face limitations in speed, resolution, and manufacturing complexity, hindering their use in high-resolution imaging applications. This study presents a universal strategy for fabricating PD arrays with vertical structures using SiO_2-assisted photolithography and etching. The resulting 10×10 self-powered PD array, composed of a simple Au/PbI_2/ITO structure, operates effectively without an external power supply. The microstructure of the patterned PbI_2 films and their photodetection properties are thoroughly characterized, showing an impressive on/off ratio of 7×10^5 and rapid response times of 780 μs and 940 μs for rise and decay times under light irradiation. Notably, the self-powered PD array demonstrates excellent imaging capability, producing clear images under 450-nm laser irradiation at varying optical power densities. The low-complexity fabrication method, which exhibits high repeatability, can be applied to other material systems and is expected to expand the potential of PDs in advanced integrated optoelectronic systems.

Keywords: self-powered detection, high-resolution photodetector, optoelectronic imaging, vertical structures

PACS: 42.79.Pw, 81.05.Je, 85.60.Gz, 85.60.Bt

DOI: 10.1088/1674-1056/ae29fc **CSTR:** 32038.14.CPB.ae29fc

1. Introduction

Photodetectors (PDs) play a vital role in various fields, including optical communications, image sensing,[1–3] and medical detection,[4] by converting optical signals into electrical signals.[5–8] With the rapid growth of artificial intelligence technologies such as machine vision,[9,10] intelligent medical imaging, robotics,[11,12] and autonomous vehicles,[13–15] the demand for high-pixel-count, low-cost PD arrays has surged.[16,17] These arrays are crucial for acquiring two-dimensional (2D) imaging data, highlighting the importance of developing large-scale PD arrays.[18,19] However, traditional PD arrays are typically based on planar interdigital electrode structures,[20–22] where the active layer is deposited onto a prefabricated electrode pattern. This design leads to limitations in response speed and resolution, as the channel length is restricted by the spacing between the electrodes, affecting the performance of planar PDs.[23–26] To overcome these challenges, vertical-structure PDs have been explored, offering improved response speed and higher resolution.[27–29] A simple approach involves using a conventional photodiode structure with cross electrodes. However, when top electrodes are fabricated through metal deposition with a shadow mask, pixel misalignment can occur, particularly in high-density arrays. This misalignment, combined with optoelectronic crosstalk and parasitic currents between pixels, compromises the ability to extract information from individual pixels, thereby reducing imaging accuracy.[30–33] Although stacking a blocking diode monolithically can address crosstalk issues, such designs require complex fabrication processes, which pose challenges in terms of device complexity and scalability. Furthermore, energy level mismatches between diodes often lead to slow carrier extraction and increased dark current, which limits the performance of the PD arrays.

In this work, we propose a universal strategy for fabricating vertical-structure PD arrays by combining etching technology with traditional micro/nano processing techniques. We demonstrate the feasibility of this approach by fabricating a 10×10 self-powered PD array with a simple Au/PbI_2/ITO structure. The device operates in self-powered mode due to its built-in electric field, exhibiting an impressive on/off ratio of 7×10^5 and rapid response times of 780 μs and 940 μs under light irradiation. Additionally, the uniformity and light stability of the array enable clear imaging of incident light distributions. This strategy is versatile, capable of being extended to other material systems and high-density PD arrays, offering a low-complexity method for large-scale integration in optoelectronic systems. Our work demonstrates significant potential for advancing high-resolution, self-powered PD arrays in

†Corresponding author. E-mail: zhuxiaoli@hnu.edu.cn
‡Corresponding author. E-mail: anlian.pan@hnu.edu.cn

© 2026 Chinese Physical Society and IOP Publishing Ltd. All rights, including for text and data mining, AI training, and similar technologies, are reserved.

CPB Online In-Press

next-generation imaging applications.

2. Methods

2.1. Materials

All chemicals were used as received without further purification. PbI_2 powder with a purity of 99.999% was purchased from p-OLED Co., Ltd. (Xi'an). Isopropanol solution (C_3H_8O, IPA) with a purity of 99.9% was purchased from Alfa Aesar Co., Ltd. (Shanghai). Acetone solution (CH_3COCH_3) with a purity of 99.9% was acquired from Sinopharm Chemical Reagent Co., Ltd. Platinum (ITO) target with a purity of 99.99% was supplied by Jiuyue New Materials (Hebei). Photoresist NYD-3000 with a purity of 99% and the developer RD6 with a purity of 99% were both obtained from Yancai Micro-Nano Technology Co., Ltd. (Suzhou).

2.2. Fabrication of vertical PD arrays

A universal fabrication method for self-powered PD arrays based on a vertical Au/PbI_2/ITO structure: First, the bottom Au electrode array (10-nm Ni/50-nm Au) pattern was fabricated via UV lithography technique (MIDAS MDA-400M) and vacuum thermal evaporation. This array consisted of 100 electrodes, with the electrode width and electrode lead width being 70 μm and 15 μm, respectively. Then, a dense SiO_2 layer was deposited via the PECVD method (Plasmalab 800Plus), which had a thickness of 100 nm; the growth temperature was 206 °C and the growth rate was 0.95 nm/s during the deposition. ICP (Plasmalab System13) was used to precisely etch the SiO_2 layer, exposing the bottom electrode array (etching rate 0.95 nm/s). Alignment lithography was performed to pattern 100 rectangle patterns on the prefabricated interdigital electrodes, where the size of each rectangle pattern was 100 μm×100 μm. The patterned PbI_2 films were prepared using a dual-source evaporation coating system (CY-1800X-SPC-4D, Chengyue Scientific Instruments). Temperature regulation was achieved by adjusting the current, thereby controlling the evaporation rate of the patterned PbI_2 films. When the current was 17.4 A, the device maintained a stable vacuum state of 5.0×10^{-4} Pa with a temperature of 147 °C, corresponding to an evaporation rate of 0.06 nm/s. Subsequently, the photoresist was removed using acetone. Finally, the transparent ITO top electrode (60 nm) was fabricated via radio-frequency (RF) magnetron sputtering (PVD75, Kurt J. Lesker). During the sputtering process, the process parameters were set as follows: the sputtering power was 25 W, the argon flow rate was controlled at 30 sccm, the sputtering rate was stabilized at 0.02 nm/s, and the vacuum pressure was maintained at 0.65 Pa, thereby completing the fabrication of the top electrode.

2.3. Characterization and measurements

Field-emission scanning electron microscopy (UK) was employed to characterize the surface morphology, while x-ray diffraction (X'Pert3 Powder) θ–2θ scan with Cu Kα radiation was performed for phase analysis. Optical properties were evaluated using a UV–vis–NIR spectrophotometer (UV-3600, Shimadzu) and a steady-state/time-resolved fluorescence spectrometer (FLS980-S2S2-stm). Electrical and optoelectronic measurements were performed using a Lake Shore CPX Probe Station integrated with an Agilent-B1500 Semiconductor Device Analyzer at ambient temperature. Time-resolved photoresponse was evaluated by using 450 nm and 520 nm lasers triggered by a square-wave generator (Thorlabs ITC 4001).

3. Results and discussion

3.1. Synthesis process and characterizations of PbI_2 arrays

The synthesis process of PbI_2 arrays is illustrated in Fig. 1(a). First, patterned substrates are fabricated on precleaned glass substrates via micro-nano fabrication techniques. Thereafter, vaporization of the PbI_2 thin film was carried out in a vacuum chamber at a pressure of 10^{-4} Pa through thermal physical vapor deposition (PVD). Meanwhile, through the adjustment of the deposition rate during the vapor deposition process, PbI_2 thin films of varying qualities can be prepared. Since PbI_2 exhibits compatibility with acetone, the patterned PbI_2 arrays are obtained following the removal of the photoresist using acetone. Figure 1(b) presents SEM images of the PbI_2 film, showing that when the deposition rate is 0.06 nm/s, a dense and homogeneous PbI_2 film is formed. Fig. S1 (in the supporting information) compares the PbI_2 thin films prepared at different deposition rates. At a deposition rate of 0.1 nm/s (a relatively high rate), the PbI_2 film exhibits leaf-like structures with many irregularly shaped microcrystals. When the deposition rate is reduced to 0.01 nm/s, top-view scanning electron microscopy (SEM) images show that the resulting PbI_2 thin film exhibits non-uniform deposition. These results indicate that the deposition rate has a critical impact on the quality of PbI_2 thin films. As shown in Fig. S2, the optical images of PbI_2 films with different patterns and precision, as well as SEM images of a PbI_2 film patterned with the school motto using various photomasks, are presented. This demonstrates that the method can produce patterned lead iodide thin films with shapes ranging from microscopic to macroscopic scales, confirming the feasibility and versatility of the synthesis approach. Furthermore, this process lays the foundation for fabricating high-pixel materials to meet the processing requirements of photodetectors (PDs). Figure 1(c) shows the x-ray diffraction (XRD) patterns of the PbI_2 film,

CPB Online In-Press

revealing four distinct peaks corresponding to the (001), (002), (003), and (004) crystallographic planes of PbI_2. These peaks match the standard card (JCPDS: 07-0235), confirming the pure PbI_2 phase.[34] The sharp and strong XRD peaks indicate that the as-prepared films possess high crystallinity.[35–37] Figure 1(d) displays the UV–vis absorption and photoluminescence (PL) spectra of the PbI_2 film. The steady-state PL spectrum shows a single peak at 515 nm, consistent with previous reports.[38] The absorption cut-off wavelength of PbI_2 is approximately 523 nm. The band gap of the PbI_2 film is calculated using the Kubelka–Munk (KM) transformation of the UV–vis spectra:

$$F(R)h\nu^2 = A(h\nu - E_g), \tag{1}$$

where $F(R)$ is the diffuse reflectance spectrum, h is Planck's constant, and ν is the frequency.[39] The calculated band gap of the PbI_2 film is approximately 2.38 eV (Fig. 1(e)), which is in good agreement with previously reported values.

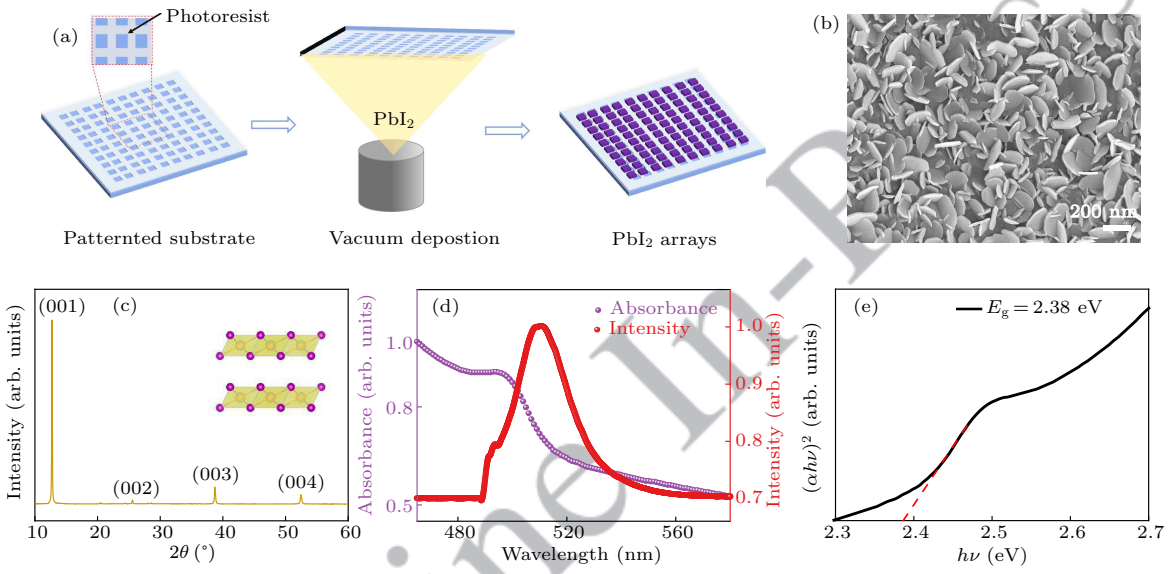


Fig. 1. (a) Schematic illustration of synthesis process of PbI_2 arrays. (b) SEM images of PbI_2 film. (c) XRD diffraction measurements of as-synthesized PbI_2 arrays. (d) UV–vis absorption and photoluminescence spectra of PbI_2 film. (e) KM transformation of UV–vis absorption spectra to the band gap.

3.2. Characterization of assembly and optoelectronic performance of self-powered PD arrays

Based on the fabricated PbI_2 thin film, a large-scale vertical PD array is assembled. To address the challenges posed by the top and bottom electrodes, we introduced a dense SiO_2 film layer between them. Figure 2(a) illustrates the schematic process of the device fabrication. The bottom electrode array is first patterned, followed by the growth of the SiO_2 film via plasma-enhanced chemical vapor deposition (PECVD). Next, inductively coupled plasma (ICP) etching is applied to precisely pattern and expose the desired sites for PbI_2 array growth. The PbI_2 thin film is then deposited by physical vapor deposition (PVD), and ITO is finally deposited using magnetron sputtering. The critical step in this process is the precise etching of SiO_2 to define the PbI_2 deposition sites. The schematic structure of the integrated device is shown in Fig. 2(b). The bottom electrode array pattern is depicted in Fig. 2(c), and figure 2(d) presents an optical image of the device after PbI_2 deposition, with the inset showing SEM images of the PD arrays and magnified views of a single device, demonstrating its regular shape and smooth surface. Figure 2(e) shows the optical image of the 10×10 pixelated PD array on a glass substrate. Figure 2(f) provides a schematic diagram for photoresponse characteristics testing. The energy levels and carrier transport processes within the device are shown in Fig. 2(g). Incident light passes through the top ITO electrode and is absorbed by the PbI_2 active layer. The work function of ITO (4.7 eV) is close to the conduction band of PbI_2, facilitating efficient electron transport, while the work function of Au (5.1 eV) aligns with the valence band of PbI_2, enabling efficient hole transport.[2,40–42] This simple structural design ensures good electrical transport under illumination, resulting in robust photovoltaic performance.

The photoresponse characteristics of the PD arrays were systematically investigated through current–voltage (I–V) measurements of each pixel. Figure 3(a) shows the I–V curves of the designed PD under dark conditions, as well as under 450-nm and 520-nm laser irradiation, with an optical power density of 4.62 mW·cm^{-2}. It is observed that the PD exhibited a low dark current and demonstrated a prominent open-circuit voltage (V_{OC}) and short-circuit current (I_{SC}), even at low power densities. Notably, the device shows a stronger response at a light wavelength of 450 nm compared to 520 nm, which can be attributed to the direct bandgap absorption of PbI_2 at its band gap of 2.38 eV. Figure 3(b) illustrates the I–V curves of the device under varying light intensities at

CPB Online In-Press

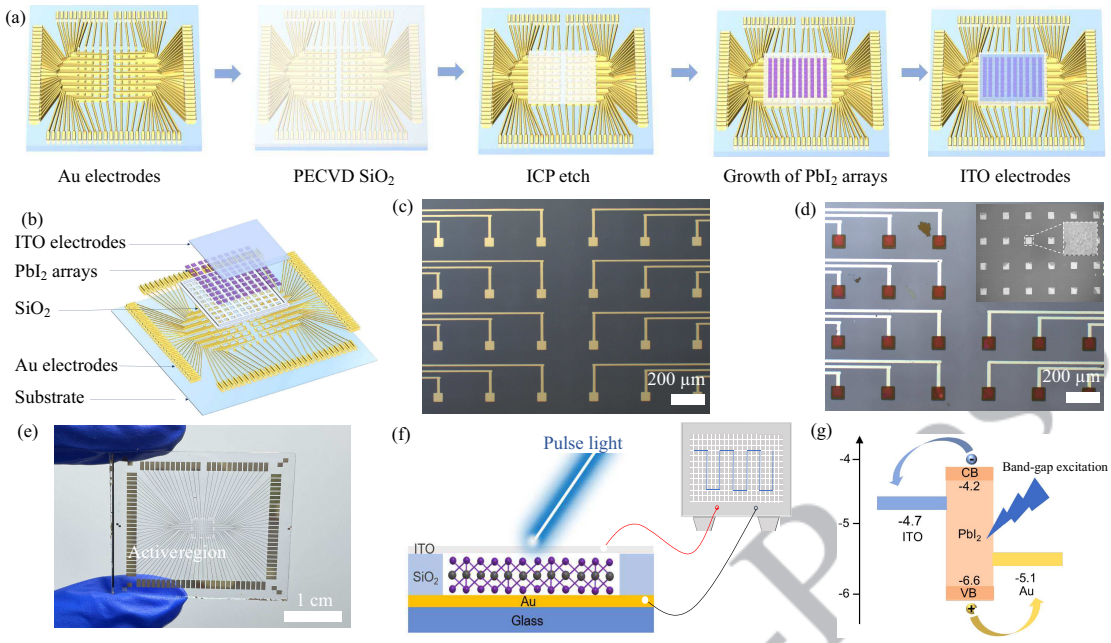


Fig. 2. (a) Schematic illustration of the device fabrication process. (b) Schematic structure of the self-powered PD arrays. (c) Optical images of the circuit with Au electrodes. (d) SEM image of the PD arrays and enlarged SEM image of a single PD in device. (e) Optical images of 10×10 pixelated self-powered PD arrays. (f) The energy levels and carrier transport process schematic diagram of the device. (g) Schematic illustration of the self-powered PD arrays optoelectronic characteristics measurement.

450 nm. As the light intensity increases, the current gradually increases, and the photovoltaic effect becomes more pronounced due to the growing number of generated electron–hole pairs. A similar trend is observed under 520-nm laser illumination (Fig. S3). As the light intensity increases, the open-circuit voltage also rises and eventually reaches a saturation value. Figure 3(c) presents the dependence of V_{OC} on illumination power density. At a power density of 4.62 mW·cm^{-2}, the maximum V_{OC} of the device reaches 0.44 V, indicating good self-powered optical detection performance. In Fig. 3(d), the time-resolved light response under 0-V bias at different incident power densities is shown, illustrating excellent optical switching characteristics in the self-powered mode. When the laser is periodically turned on and off, the I_{SC} rises and falls correspondingly. It can also be observed that the saturation level increases gradually as the optical power density increases, leading to a higher number of electron–hole pairs, while the dark current remains relatively low, indicating good cutoff performance. Moreover, under the same light intensity, the on-state current of the device under 520-nm laser irradiation is lower than that under 450-nm irradiation (Fig. S4), which can be attributed to the superior absorption of PbI_2 at 450 nm. Figure S5 shows the optical switching characteristics by varying the timing and period of the pulsed laser. The results indicate that the self-powered PD exhibits stable light response under different illumination intensities and pulsed laser conditions. Additionally, a comparison device was fabricated by reducing the deposition thickness of PbI_2, and electrical tests were conducted on it (see Figs. S6 and S7). The results show that the optical response of the thinner PbI_2 device was inferior to that of the original device. This can be attributed to the fact that thicker PbI_2 films can absorb more light and generate more charge carriers under a given light intensity, resulting in a larger output current. However, as the thickness increases, the active layer also represents the channel length of the vertical structure, meaning that excessively thick films can reduce the output current due to the increased channel resistance. The response and decay times were calculated by measuring the time taken to reach 10% and 90% of the maximum photocurrent. As shown in Fig. 3(e), the response time and decay time are calculated to be 780 μs and 940 μs, respectively, which are significantly faster than the corresponding values of photodetector (PD) arrays based on other materials and structures. Moreover, compared with Si-based self-powered devices, it not only features low process complexity but also exhibits prominent performance advantages (see Tables S1 and S2). It is also observed that the photocurrent of the device decays faster when a bias is applied. Fig. S8 shows the optical switching stability characteristics of the device at 0-V and 1-V biases, where noticeable attenuation occurs under a 1-V bias. Compared to the previously reported PbI_2 array PDs, the PD reported in this work shows faster photoresponse characteristics. The dependence of the photocurrent (I_{ph}) and detectivity (D^*), as key figures-of-merit of photodetectors, was calculated and presented in Fig. 3(f). These properties were calculated using the following equation:[43,44]

$$I_{ph} = I_{light} - I_{dark}, \tag{2}$$

$$R = \frac{I_{ph}}{PS}, \tag{3}$$

CPB Online IOP

$$D^* = \frac{RS^{1/2}}{(2qI_{\text{dark}})^{1/2}}, \tag{4}$$

$$I_{\text{ph}} = \alpha P^{\beta}, \tag{5}$$

where I_{light} is the photocurrent, I_{dark} is the dark current, R is the responsivity; S is the effective area of an individual pixel, and q is the elementary charge; α is a constant, P is the optical intensity, β is an index related to the photoresponse of the corresponding optical power density. The best-fitting value of β is 0.85, exhibiting a sublinear power-law behavior. Furthermore, the detectivity (D^*) decreases as illumination intensity increases and its value is approximately 6.3×10^{10} Jones at an illumination intensity of 40 μW·cm^{-2}, implying an outstanding low-light detection capability in the self-powered mode.

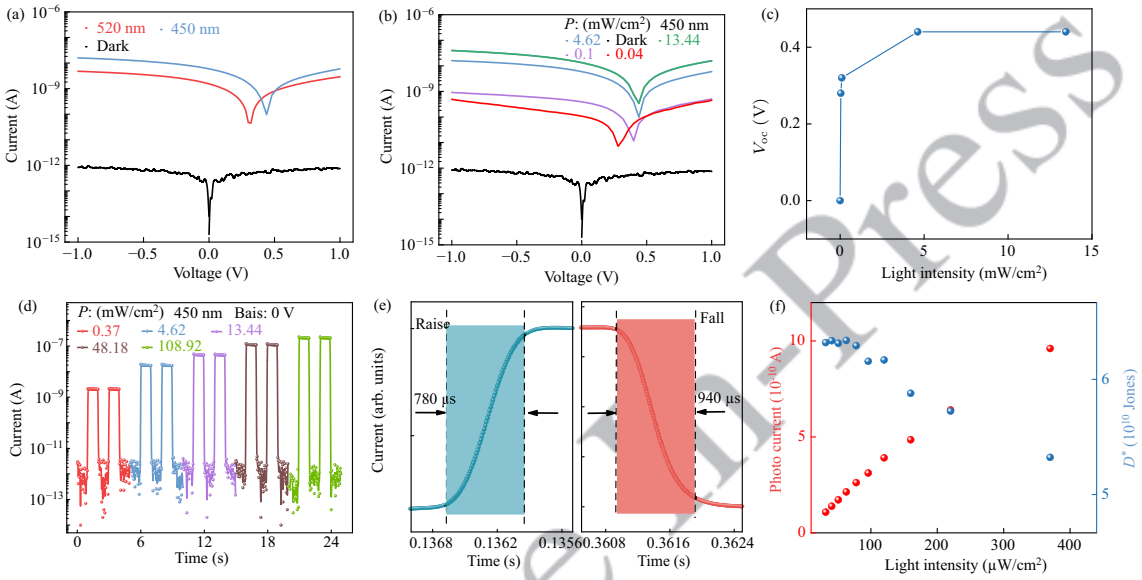


Fig. 3. (a) Light source with different wavelengths (4.62 mW·cm^{-2}). (b) With incident light power density from 0 to 13.44 mW·cm^{-2} (wavelength: 450 nm). (c) The V_{OC} statistics of single device under 450-nm laser illumination with different light intensities. (d) Photoswitching property of single device at different light intensities with 0-V bias. (e) The response and decay time under 450-nm laser illumination with light intensity of 48.18 mW·cm^{-2} with 0 bias. (f) Dependence of the photocurrent and detectivity at 0-V bias.

3.3. Application of self-powered PD arrays in high-resolution optical imaging

The imaging capability of the self-powered PD array was further characterized.[45] Given the simple vertical device structure of the self-powered PD array and its compatibility with standard lithography and etching technologies, the device holds great potential for imaging applications. In imaging tasks, each individual PD functions as a pixel, and the stability and uniformity of the photoelectric characteristics of each pixel are critical for overall imaging performance. Figure 4(a) shows the long-term optical switching stability of the device at 0-V bias. After continuous operation for 4000 seconds (2.3×10^6 cycles), the device exhibits excellent switching characteristics, with only a slight attenuation in photocurrent, indicating good stability. To assess the uniformity of the photoresponse across all pixels in the array, Fig. S9 displays the photocurrent measurements of 100 pixel points under both dark and illuminated states in self-powered mode. The currents in both dark and light conditions are distributed within a narrow range, demonstrating that the self-powered PD array exhibits excellent pixel homogeneity. To further illustrate this uniformity, a 2D contrast map showing the light and dark current distribution of 100 pixels is provided in Fig. S10. Figure 4(b) presents the light-to-dark ratio across all pixels, revealing that the $I_{\text{on}}/I_{\text{off}}$ ratio remains consistently high, indicating uniform photoresponse. To evaluate the imaging capability of the self-powered PD array, a prototype experiment was conducted based on the imaging principle. A pre-designed shadow mask was placed between the light source and the device. As light passed through the mask, the pixels covered by the mask remained in the dark state, while the incident light illuminated the pixels in the unmasked areas. The output current from each pixel was mapped to reconstruct the input image, as shown in Fig. 4(c). When light passed through the pre-designed shadow mask, speckle spots were formed on the pixels of the self-powered PD array. The pixels under illumination have higher current values, while the others blocked by the shadow mask show no light response. We used a mask of "heart" to obtain the 2D planar graph as shown in Figs. 4(d)–4(f) and S11. A clear pattern of "heart" could be identified from the mapping results, and the resulting pattern was consistent with the pattern of light spots, indicating that each pixel of the self-powered PD array could work independently and had basic light intensity response ability. Meanwhile, in weak-light conditions, this self-powered photodetector array is capable of effectively identifying the target contour.

CPB Online in Press

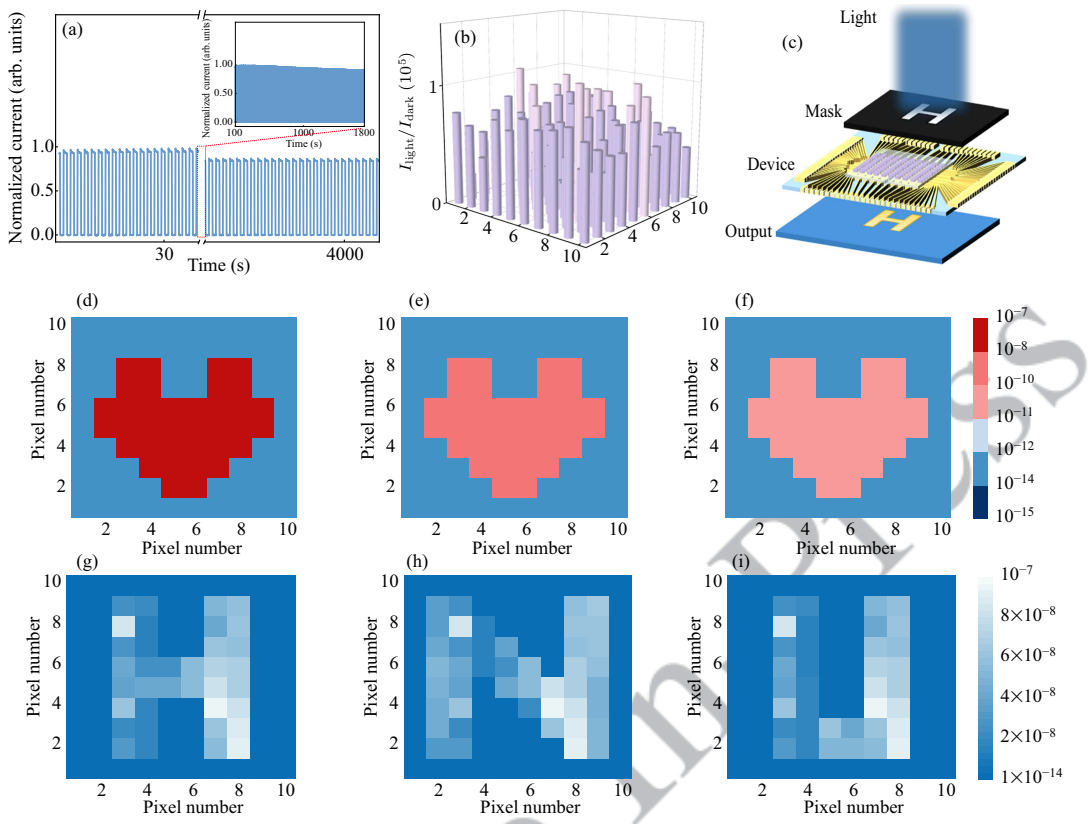


Fig. 4. (a) The long-term optical switching stability characteristics of the single device with 0-V bias (wavelength: 450 nm, 48.18 mW·cm^{-2}). (b) The three-dimensional (3D) diagram of the I_{on}/I_{off} ratio for each pixel device. (c) Schematic illustration of the self-powered PD arrays to detect multipoint light distribution. (d)–(f) The "heart" pattern photocurrent image obtained with different illumination intensities. (g)–(i) Imaging results of the device with "H", "N", "U" shaped masks respectively.

Moreover, as the light intensity increases, the contrast also increases with the color deepening to further enhance contrast. Additionally, the 10×10 photodetector array was used to image different patterns. Masks shaped as "H", "N", and "U" were employed to produce the corresponding 2D images shown in Figs. 4(g)–4(i). The resulting images clearly depict the letters "H", "N", and "U", and the patterns obtained matched the light spot pattern precisely, confirming the device's ability to reliably image a variety of patterns.

4. Conclusion and perspectives

In summary, we have developed a universal fabrication method for vertical-structure photodetectors, integrating etching techniques with traditional micro-nano processing to enable the array integration of these devices. The simple structure design of Au/PbI_2/ITO validates the feasibility of this fabrication approach. The self-powered photodetector exhibits impressive photoresponse performance, with a large on/off current ratio (up to 10^5), fast rise/decay times of 780 μs and 940 μs, and excellent long-term working stability. Moreover, this fabrication method is compatible with a range of material systems and can be applied to various optoelectronic devices. This approach holds great promise for advancing the development of array-based optoelectronic devices for large-scale patterning and high-resolution imaging applications.

Acknowledgements

Project supported by the National Natural Science Foundation of China (Grant Nos. 62375081, U22A20138, 52372146, 62090035, and 52221001) and the National Key Research and Development Program of China (Grant Nos. 2022YFA1204300 and 2022YFA1402501).

References

[1] Zhao Z P, Liu J G, Liu Y and Zhu N H 2017 *J. Semicond.* **38** 121001
[2] Wu L Y, Shi X N, Fan H B, Li Q J, Hu P and Teng F 2025 *Chin. Phys. B* **34** 088501
[3] Liu J, Liu P L, Chen D Y, Shi T L, Qu X X, Chen L, Wu T, Ke J P, Xiong K, Li M Y, Song H S, Wei W, Cao J K, Zhang J B, Gao L and Tang J 2022 *Nat. Electron.* **5** 443
[4] Chen P Y, Chen M M, Huang J X, Li G P, Zhang H M, Zhang C L, Liu Y and Cao D W 2024 *Appl. Phys. Lett.* **125** 103301
[5] Zhang J F, Ding Z Y, Liu Z W, Li G J, Kwok H S and Liu Y 2025 *Small Methods* **9** 2401011
[6] Li W, Yang R J, Han X, Cheng L, Yin T L, Gao K X, Gan X T, Wang Y C and Wang S X 2025 *Small* **21** 2408379
[7] Lan C Y, Dong R T, Zhou Z Y, Shu L, Li D P, Yip S P and Ho J C 2017 *Adv. Mater.* **29** 1702759
[8] Liu D, Chen R C, Liu F J, Zhang J, Zhuang X M, Yin Y X, Wang M X, Sa Z X, Wang P, Sun L, Peng Z Y, Tan Y, Jia Z T, Chen M and Yang Z X 2022 *ACS Appl. Mater. Interfaces* **14** 46748
[9] Tang Y, Cai Q, Yang L H, Dong K X, Chen D J, Lu H, Zhang R and Zheng Y K 2017 *Chin. Phys. B* **26** 038503
[10] He T, Ma H, Wang Z, Li Q, Liu S N, Duan S K, Xu T F, Wang J C, Wu H T, Zhang F, Ye Y T, Wu J H, Li S, Zhang K, Martyniuk P, Rogalski A, Wang P, Li L, Lin H T and Hu W D 2024 *Nat. Photonics* **18** 60

CPB Online in Press

[11] Li D Y, Li Z X, Pan C, Sun Y, Zhou J, Yangdong X J, Xu X, Liu L X, Wang H Y, Chen Y X, Song X Y, Liu P B, Zhou X, Liang S J, Miao F and Zhai T Y 2024 *Adv. Mater.* **36** 2406984

[12] Yang Z O, Huang X Z, Liu Y, Wang Z, Zhang Z W, Ma B Y, Shang H L, Wang L Z, Zhu T, Duan X D, Hu H L and Yue J L 2024 *Small Methods* **9** 2401259

[13] Li D Y, Li Z X, Sun Y, Zhou J, Xu X, Wang H Y, Chen Y X, Song X Y, Liu P B, Luo Z T, Han S T, Zhou X and Zhai T Y 2024 *Adv. Mater.* **36** 2407010

[14] Ao Z K, Liu C, Ma H F, Lan X, Zhang J H, Zhang B H, Zhang F, Wang Z R, Chen P, Zhong M Z, Wang G and Zhang Z W 2024 *Small* **20** 2404897

[15] Zhang B H, Ao Z K, Lan X, Zhong J, Zhang F, Zhang S H, Yang R F, Wang L Y, Chen P, Wang G, Yang X D, Liu H, Cao J H, Zhong M Z, Li H J and Zhang Z W 2024 *Nano Lett.* **24** 7716

[16] Yao Z T, Xiong Y T, Kang H Y, Xu X Z, Guo J H, Li W and Xu X B 2024 *ACS Omega* **9** 2606

[17] Xu X Z, Liu W F, Ji Z K, Hao D D, Yan W Y, Ye Z L, Hu Y, Fang M H, Wang C C, Ma L, Huang J, Xu X B and Weiss P S 2021 *ACS Materials Lett.* **3** 1189

[18] Ma M G, Chen H H, Zhou K N, Xie C, Liang Y, Wang L, Wu C Y, Yang W H, Guo J W and Luo L B 2021 *J. Mater. Chem. C* **9** 2823

[19] Jin K K, Long J H, Chang H X, Su R T, Zhang J Y, Chen S Y, Ma Y X and Zhou P 2024 *Chin. Phys. B* **33** 074201

[20] Wang T, Zheng D M, Vegso K, Mrkyvkova N, Siffalovic P, Yuan X C, Somekh M G, Coolen L, Pauporte T and Fu F 2023 *Nano Energy* **116** 108827

[21] Wu W Q, Wang X D, Han X, Yang Z, Gao G Y, Zhang Y F, Hu J F, Tan Y W, Pan A L and Pan C F 2019 *Adv. Mater.* **31** 1805913

[22] Huang L L, Wang B, Shuai Q, Wang Q Y, Wang X, Liu Y, Yuan W J, Liu H W, Zhu X L, Chen Y W, Duan H G, Li D and Pan A L 2025 *Sci. China Mater.* **68** 2308

[23] Lu Q C, Zhang Y F, Yang G L, Xiong M L, Wu W Q, Xu Z S, Lu H, Liang Y G, He Z P, Yu Y, Mo X M, Han X and Pan C F 2023 *Small* **19** 2300364

[24] Lin L, Liu Y, Wu W Q, Huang L L, Zhu X L, Xie Y F, Liu H W, Zheng B Y, Liang J Y, Sun X X, Zhu C G, Wu G C, Shuai Q, Huang Z R, Wang T H, Li D and Pan A L 2023 *Adv. Electron. Mater.* **9** 2300106

[25] Deng W, Jie J, Xu X Z, Xiao Y L, Lu B, Zhang X J and Zhang X H 2020 *Adv. Mater.* **32** 1908340

[26] Liu Y, Wang B, Wu L, Huang L L, Lin L, Xiang L, Liu D Q, Zhang S G, Zhu C G, Tao Y J, Li D and Pan A L 2023 *ACS Appl. Mater. Interfaces* **15** 51380

[27] Liang Y G, Lu Q C, Wu W Q, Xu Z S, Lu H, He Z P, Zhu Y Z, Yu Y, Han X and Pan C F 2023 *Small Methods* **7** 2300339

[28] Zhou H, Song Z N, Grice C R, Chen C, Zhang J, Zhu Y F, Liu R H, Wang H and Yan Y F 2018 *Nano Energy* **53** 880

[29] Xu Z S, Han X, Wu W Q, Li F T, Wang R, Lu H, Lu Q C, Ge B H, Cheng N Y, Li X Y, Yao G J, Hong H, Liu K H and Pan C F 2023 *Light: Sci. Appl.* **12** 2047

[30] Zhao Y, Li C L and Shen L 2018 *Chin. Phys. B* **27** 127806

[31] Intonti K, Pelella A, Neill H, Patil V, Hurley P K, Ansari L, Gity F and Bartolomeo A D 2024 *Appl. Phys. Lett.* **125** 173505

[32] Wang D, Wang X Y, Pan Y, Bian J H, Liu K, Guo J, Lin J M, Sun Z B, Gou S, Sheng C M, Dong X Q, Su H S, Zhu Y X, Sun Q C, Xu Z H, Guo A Y, Shao L, Chen H L and Bao W Z 2024 *Adv. Opt. Mater.* **12** 2400547

[33] Zhan Z Y, Lin D X, Cai J T, Lu Y H, Chen A D, Zhang T J, Chen K, Liu P Y, Wang X M and Xie W G 2022 *Adv. Mater.* **34** 2207106

[34] Hu W, Huang W, Yang S Z, Wang X, Jiang Z Y, Zhu X L, Zhou H, Liu H J, Zhang Q L, Zhuang X J, Yang J L, Kim D H and Pan A L 2017 *Adv. Mater.* **29** 1703256

[35] Li Z L, Li Q J, Li H Y, Tian F Y, Du M Y, Fang S X, Liu R, Zhang L J and Liu B B 2022 *Small Methods* **6** 2201044

[36] Popov G, Mattinen M, Hatanpää T, Vehkamäki M, Kemell M, Mizohata K, Räisänen J, Ritala M and Leskelä M 2019 *Chem. Mater.* **31** 1101

[37] Liu J Q, Liang Z H, Xu B, Xiang H, Xia Y D, Yin J and Liu Z G 2016 *RSC Adv.* **6** 59445

[38] Zhong M Z, Zhang S, Huang L, You J B, Wei Z M, Liu X F and Li J B 2017 *Nanoscale* **9** 3736

[39] Qin Y, Li L H, Yu Z A, Wu F G, Dong D N, Guo W, Zhang Z F, Yuan J H, Xue K H, Miao X S and Long S B 2021 *Adv. Sci.* **8** 2101106

[40] Deng W, Jie J S, Xu X Z, Xiao Y L, Lu B and Zhang X H 2020 *Adv. Mater.* **32** 1908340

[41] Wu D, Xu M M, Zeng L H, Shi Z F, Tian Y Z, Li X J, Shan C X and Jie J S 2022 *ACS Nano* **16** 5545

[42] Tian W, Wang Y D, Chen L and Li L 2017 *Small* **13** 1701848

[43] Xie C, Mak C H, Tao X M and Yan F 2017 *Adv. Funct. Mater.* **27** 1603886

[44] Li L D, Ye S, Qu J F, Zhou F F, Song J and Shen G Z 2021 *Small* **17** 2005606

[45] Pan S Q, Wu S E, Hei J J, Zhou Z W, Zeng L H, Xing Y K, Lin P, Shi Z F, Tian Y T, Li X J and Wu D 2023 *Nano Res.* **16** 10552

CPB Online First